

# CBCT-Based Synthetic CT Generation Using Conditional Flow Matching Model

Junbo Peng<sup>1</sup>, Huiqiao Xie<sup>1</sup>, Tonghe Wang<sup>2</sup>, Xiangyang Tang<sup>3</sup>, and Xiaofeng Yang<sup>1,\*</sup>

<sup>1</sup>Department of Radiation Oncology and Winship Cancer Institute, Emory University, Atlanta, GA 30322

<sup>2</sup>Department of Medical Physics, Memorial Sloan Kettering Cancer Center, New York, NY, 10065

<sup>3</sup>Department of Radiology and Imaging Sciences, Emory University, Atlanta, GA 30322

\*Email: xiaofeng.yang@emory.edu

## Abstract

**Background:** Daily or weekly cone-beam computed tomography (CBCT) is employed in image-guided radiotherapy (IGRT) for precise patient alignment, which is a promising candidate for adaptive radiotherapy (ART) replanning. However, its clinical utility in quantitative tasks, including organ segmentation and dose calculation, is hindered by severe artifacts and inaccurate Hounsfield unit (HU). To facilitate the implementation of online ART in clinical settings, it is essential to enhance CBCT image quality to a level comparable with that of conventional CT scans.

**Purpose:** This purpose of this study is to develop a conditional flow matching model for synthetic CT generation from CBCT with enhanced image quality.

**Methods:** The study proposed a conditional flow matching model that gradually transforms a sample from normal distribution to the corresponding CT sample conditioned on the input CBCT image. The proposed model was trained using CBCT and deformed planning CT (dpCT) image pairs in a supervised learning scheme. The feasibility of the conditional flow matching model was verified using studies of brain, head-and-neck (HN), and lung patients. The quantitative performance was evaluated using three metrics, including mean absolute error (MAE), peak signal-to-noise ratio (PSNR), and normalized cross-correlation (NCC). The proposed flow matching model was also compared to other flow matching and diffusion-based generative models for sCT generation.

**Results:** The proposed flow matching model effectively reduced multiple types of artifacts on CBCT images in all the studies. In the study of brain patient, the MAE,

PSNR, and NCC of the sCT were improved to 26.02 HU, 32.35 dB, and 0.99, respectively, from 40.63 HU, 27.87 dB, and 0.98 on the CBCT images. In the study of HN patient, the metrics were improved to 33.17 HU, 28.68 dB, 0.98 from 38.99 HU, 27.00 dB, 0.98. In the lung patient study, the metrics were 25.09 HU, 32.81 dB, 0.99 and 32.90 HU, 30.48 dB, 0.98 for sCT and CBCT, respectively.

**Conclusions:** The proposed conditional flow matching model effectively synthesizes high-quality CT-like images from CBCT, achieving accurate HU representation and artifact reduction. This enables more reliable organ segmentation and dose calculation in CBCT-guided online ART workflows.

**Keywords:** CBCT, Flow Matching Model, Synthetic CT

# Contents

<b>1</b>	<b>Introduction</b>	<b>4</b>
<b>2</b>	<b>Materials and Methods</b>	<b>5</b>
2.1	Image Acquisition and Preprocessing . . . . .	5
2.2	Flow Matching Model . . . . .	5
2.3	Sampling Process . . . . .	7
2.4	Flow Matching Model for Synthetic CT Generation . . . . .	8
2.5	Comparison Studies . . . . .	9
2.6	Implementation and Evaluation . . . . .	12
<b>3</b>	<b>Results</b>	<b>12</b>
3.1	Improvement of Visual Quality . . . . .	12
3.2	Quantitative Analysis . . . . .	13
3.3	Comparison Studies . . . . .	13
<b>4</b>	<b>Discussion</b>	<b>18</b>
<b>5</b>	<b>Conclusions</b>	<b>20</b>

# 1 Introduction

Cone-beam computed tomography (CBCT) is extensively utilized on a daily or weekly basis in current image-guided radiotherapy (IGRT) workflows for patient alignment and treatment monitoring, helping reduce setup errors and enhance treatment precision [1]. However, compared to conventional multi-detector CT (MDCT), the CBCT images are susceptible to a range of artifacts—such as beam-hardening induced cupping, shading, streaking and scatter artifacts—that result in substantial inaccurate Hounsfield unit (HU) values [2–4]. These limitations hinder the direct use of CBCT in quantitative applications like organ segmentation and dose calculation, thus posing a barrier to fully realizing CBCT-based adaptive radiotherapy (ART). In order to circumvent these issues, current implementations of ART often rely on deforming the planning MDCT (henceforth pCT) to match CBCT anatomy for dose calculation [5]. However, the accuracy of deformable image registration is compromised by CBCT artifacts and anatomical changes during the treatment, making the process heavily dependent on operator expertise and intuitional protocols [6].

Recent research aimed at enabling direct CBCT-based ART falls into two major categories: artifact correction to enhance CBCT image quality [7–16], and synthetic MDCT (henceforth sCT) generation from CBCT that approximates the quality of pCT [6, 17–21].

In general, CBCT artifact correction methods consist of hardware-, model-, and deep learning-based approaches. The hardware-based solutions, such as anti-scatter grids [7, 22], lattice-shaped beam stoppers [9], and primary-modulation beam, help suppress scatter artifacts at a cost of compromised quantum efficiency and degraded signal-to-noise ratio [19]. The model-based techniques aim to replicate the CBCT imaging physics process to correct artifacts. For example, Monte-Carlo (MC) simulations [10] and analytical methods [14] have been developed to estimate scattering signals. While the MC methods provide high accuracy, they are computationally expensive. The analytical scatter kernel models are more efficient but less reliable in heterogeneous tissues due to the nonlinear nature of scatter [23]. Deep learning-based approaches attempt to learn the mappings from artifact-laden to artifact-free CBCT images using paired datasets. These models operate in either the projection or image domain [15, 16], and have demonstrated effectiveness in correcting scatter [16], streaking [15], and metal artifacts [24]. However, they often struggle to comprehensively address multiple artifact sources, which remains a shared limitation across all artifact correction methods.

The sCT generation approaches leverage image prior information from the pCT to map CBCT voxels to the target pCT via deep learning models including U-net and GANs [6, 17, 19–21]. Denoising diffusion models have recently emerged as a powerful generative framework that produced state-of-the-art image quality in medical imaging including the CBCT-based sCT generation [25–27]. However, the denoising diffusion models typically rely on a long sequence of iterative updates to progressively transform an initial random noise sample into a realistic image—a procedure often referred to as the sampling chain. At each iteration, the generated image is gradually refined toward higher fidelity. While this iterative mechanism underpins the strong generative performance of diffusion models, it also imposes a substantial computational burden: hundreds or even thousands of steps are often required to obtain a single high-quality sample. Consequently, the sampling process becomes both time-consuming and resource-intensive, which may constitute a practical bottleneck for ap-

plications that demand rapid image synthesis [28].

In this study, we propose a conditional flow matching framework for efficient sCT generation from CBCT images. The model is trained using paired CBCT and deformed planning MDCT (dpCT henceforth) images, where the dpCT serves as the image label and CBCT acts as the conditioning image input. During inference, a white Gaussian noise sample is transformed in several steps into an sCT image conditioned on the CBCT. With only 5–20 sampling steps, our method achieves comparable performance to a conventional DDPM with 1000 steps, while substantially reducing inference time and computational cost. Experimental results on brain, head-and-neck (HN), and lung datasets demonstrate that the proposed method can efficiently generate sCT with improved HU accuracy and reduced artifacts, thereby supporting the feasibility of direct CBCT-based ART.

## 2 Materials and Methods

### 2.1 Image Acquisition and Preprocessing

In this study, the CBCT and pCT images were acquired from 41 brain, 47 HN patients, and 37 lung patients at our institutional center. For the brain cohort, training and testing datasets consist of 4682 slices from 30 patients and 500 slices randomly selected from 11 patients, respectively. In the HN patient study, 4314 slices from 37 patients were used for training, with 500 random slices from other 10 patients were used for testing. For the lung cohort, the training set included 3216 slices from 27 patients and the testing set consist of 500 random slices from other 10 patients. All CT images were acquired at 120 kVp using the Siemens SOMATOM Definition AS scanner. All CBCT images were acquired using the Varian TrueBeam system. For the brain and HN cohort, CBCT images were acquired at 100 kVp, while the lung CBCT images were acquired at 125 kVp. Both CT and CBCT volumes had isotropic voxel dimensions of  $1.0 \times 1.0 \times 1.0 \text{ mm}^3$ . The pCT images were deformably registered and resampled to align with the original CBCT images using a commercial software (Velocity AI version 3.2.1), ensuring matched volume size and voxel spacing across image pairs. The body contours extracted from both modalities were combined and applied uniformly to the corresponding CBCT and pCT scans. Prior to inputting into the neural networks, images were cropped to  $256 \times 256$  pixels (brain and HN patients) and  $512 \times 272$  (lung patients) and intensity normalized to the range of  $[-1, 1]$ .

### 2.2 Flow Matching Model

Let  $\mathbb{R}^d$  denote the data space, where each data point is given by  $x = (x_1, \dots, x_d) \in \mathbb{R}^d$ . The probability density path  $p : [0, 1] \rightarrow \mathbb{R}^d \rightarrow \mathbb{R}_{>0}$  is a family of time-dependent probability density functions that satisfies  $\int p_t(x) dx = 1$ . A time-dependent vector field  $v : [0, 1] \rightarrow \mathbb{R}^d \rightarrow \mathbb{R}^d$  can be used to construct a time-dependent diffeomorphic map, known as a flow,  $\psi : [0, 1] \rightarrow \mathbb{R}^d \rightarrow \mathbb{R}^d$ , defined by the ordinary differential equation (ODE):

$$\frac{d}{dt}\psi_t(x) = v_t(\psi_t(x)) \quad (1)$$

$$\psi_0(x) = x \quad (2)$$

Prior work proposed parameterizing the vector field  $v_t$  with a neural network  $v_{t,\theta}(x)$ , where  $\theta \in \mathbb{R}^p$  are trainable parameters. This yields a deep parametric model of the flow  $\phi_t$  [29], referred to as a continuous normalizing flow (CNF). The CNF framework allows a simple density  $p_0$  (e.g., Gaussian noise) to be progressively transformed into a complex target distribution  $p_1$  via the push-forward relation

$$p_t = [\psi_t]_* p_0, \quad (3)$$

where the operator  $*$  is explicitly given by

$$[\psi_t]_* p_0(x) = p_0(\psi_t^{-1}(x)) \det \left[ \frac{\partial \psi_t^{-1}}{\partial x}(x) \right]. \quad (4)$$

However, the practical use of CNFs as generative models has been significantly limited by the high computational cost associated with maximum likelihood training. To overcome this drawback, the flow matching has recently been proposed as a viable alternative. The key observation underlying this approach is that any time-dependent vector field  $v_t : [0, 1] \rightarrow \mathbb{R}^d \rightarrow \mathbb{R}^d$  can be associated with the temporal evolution of a prescribed density path  $p_t : [0, 1] \rightarrow \mathbb{R}^d \rightarrow [0, \infty)$  through the fundamental continuity equation [30]

$$\frac{\partial p_t(x)}{\partial t} = -\nabla \cdot (p_t(x) v_t(x)), \quad (5)$$

where  $\nabla \cdot$  denotes the divergence operator. This equation ensures that the probability mass is conserved throughout the transformation process.

The velocity field  $v_t(x)$  is learned by a neural network  $v_{t,\theta}(x)$  that minimizes the following objective [31]:

$$\mathcal{L}_{\text{FM}} = \mathbb{E}_{t \sim \mathcal{U}[0,1], x_t \sim p_t} \left[ \|v_{t,\theta}(x_t) - v_t(x_t)\|^2 \right]. \quad (6)$$

In essence, the flow matching (FM) loss enforces the regression of the target vector field  $v_t$  by a neural network parameterization  $v_{t,\theta}$ . When the loss converges to zero, the learned CNF model recovers the desired density path  $p_t(x)$ . However, the ground truth of marginal vector field  $v_t$  is unknown in general, making the optimization problem above intractable. Instead, prior works showed that  $v_t$  could be constructed via superimposing conditional vector fields  $v_t(\cdot|x_1)$  conditioned on available training data  $x_1 \sim p_1$ . Then the conditional flow matching (CFM) objective is given as [31]

$$\mathcal{L}_{\text{CFM}} = \mathbb{E}_{t \sim \mathcal{U}[0,1], x_1 \sim p_1, x_t \sim p_t(\cdot|x_1)} \left[ \|v_{t,\theta}(x_t) - v_t(x_t|x_1)\|^2 \right]. \quad (7)$$

In expectation, the minimization of the CFM objective is equivalent to minimizing the FM objective. As a result, we can train a CNF to generate the marginal probability path  $p_t$ , which approximates the unknown data distribution  $p_1$  at  $t = 1$  without requiring explicit knowledge of either the marginal path  $p_t$  or the corresponding marginal vector field.

The CFM objective works for any conditional probability path and conditional vector field. One of the choices is known as the conditional optimal-transport (OT) path [32], which can be explicitly expressed as

$$x_t = t \cdot x_1 + (1 - t) \cdot x_0. \quad (8)$$

Then we get the implementation of FM as

$$\mathcal{L}_{\text{CFM}}^{\text{OT}} = \mathbb{E}_{t \sim \mathcal{U}[0,1], x_0 \sim p_0, x_1 \sim p_1} \left[ \left\| v_{t,\theta}(x_t) - (x_1 - x_0) \right\|^2 \right]. \quad (9)$$

The workflow of the flow-matching model is shown in Figure 1.

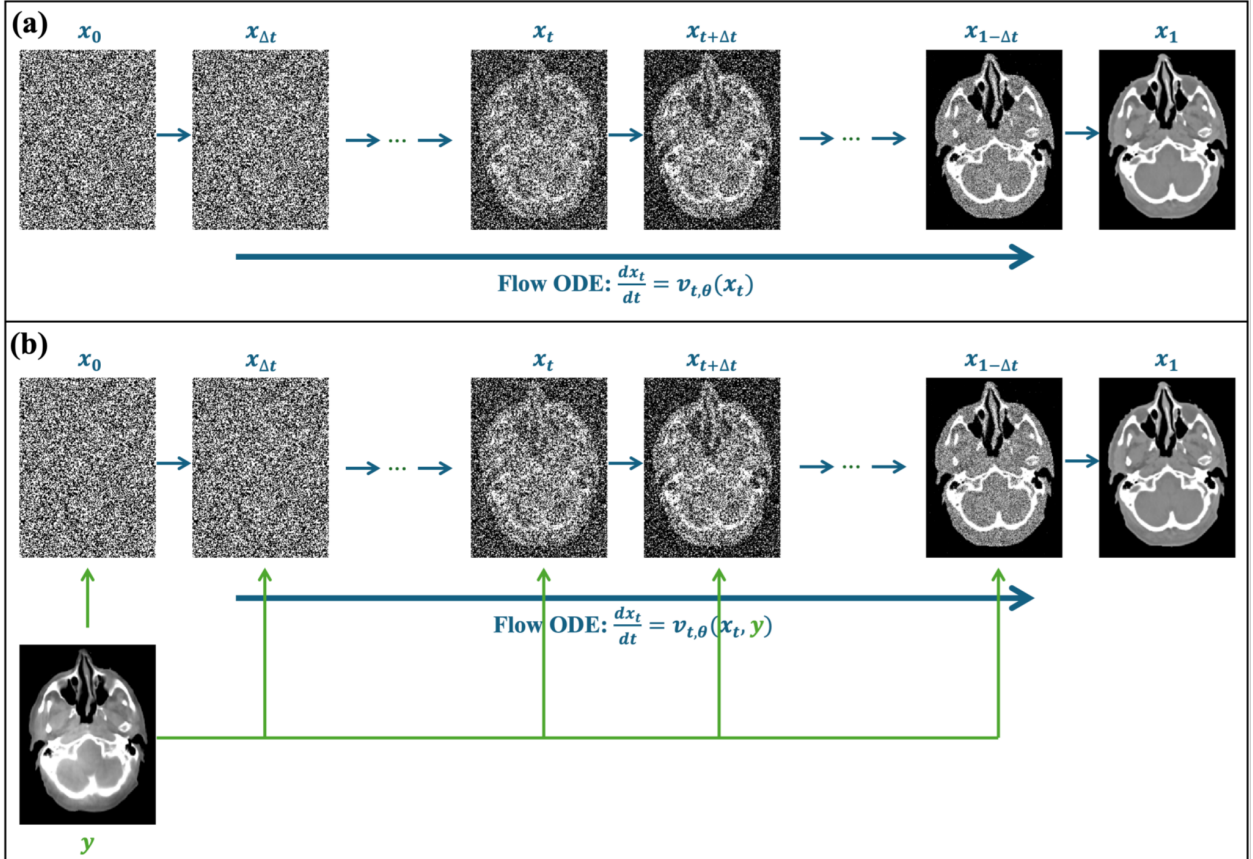


Figure 1: Workflows of (a) the standard flow matching model (Gaussian w/o Concat) and (b) the proposed conditional flow matching model (Gaussian w/ Concat) for synthetic CT generation from CBCT.

### 2.3 Sampling Process

After training the flow-based model, sample generation is performed by integrating the flow ODE forward in time. Recall that the dynamics of the learned flow are governed by

$$\frac{d}{dt} \psi_t(x) = v_t(\psi_t(x)), \quad (10)$$

$$\psi_0(x) = x, \quad (11)$$

where the initial condition  $x \sim p_0$  is drawn from a simple prior distribution such as a standard Gaussian. The final state  $\phi_1(x)$  provides a sample from the learned approximation of the target data distribution  $p_1$ .

To approximate the continuous dynamics, we discretize the unit interval  $[0, 1]$  into  $N$  equal steps. Denoting the step size by  $\Delta t = 1/N$  and the discretization grid by  $t_k = k \Delta t$  for  $k = 0, \dots, N$ , we introduce the sequence  $\{x_k\}_{k=0}^N$  to represent the numerical trajectory, where  $x_k \approx \psi_{t_k}(x)$ .

Among the various numerical integrators available, we adopt the explicit Euler method for its simplicity and efficiency. Concretely, the iteration proceeds as

$$x_{k+1} = x_k + \Delta t v_{t_k}(x_k), \quad x_0 \sim p_0. \quad (12)$$

This recursive scheme propagates the initial noise sample  $x_0$  step by step until  $x_N$ , which serves as an approximation to  $\psi_1(x)$ .

The Euler update rule may be interpreted as a sequence of incremental transport operations [33], where each step pushes the current point  $x_k$  along the learned velocity field  $v_{t_k}$ . Intuitively, this process gradually deforms the simple reference distribution  $p_0$  into the more complex data distribution  $p_1$ . From this perspective, the sampling stage realizes a discrete-time approximation of the continuous push-forward relation

$$p_t = [\psi_t]_* p_0, \quad (13)$$

where the discretization is implemented via the iterative map.

In practice, the choice of the number of steps  $N$  directly affects the trade-off between computational efficiency and fidelity of the generated samples. A larger  $N$  leads to a finer discretization of the dynamics and a more faithful approximation of the target distribution, at the expense of increased computational cost. On the other hand, a smaller  $N$  yields faster sampling but may introduce noticeable discretization bias. We observe empirically that the learned flows remain stable under moderate step sizes, and high-quality samples can often be obtained without requiring an excessively large  $N$ . This makes the Euler solver a practical and widely applicable choice for sampling in flow matching models [31, 32].

## 2.4 Flow Matching Model for Synthetic CT Generation

The original flow matching model is designed as an unsupervised framework for unconditional image generation and is therefore not directly applicable to tasks requiring semantic control over the output [34]. In contrast, CT synthesis from CBCT falls under the category of conditional image-to-image generation, where the generated sCT must correspond to a specific input CBCT rather than being a random sample from the target CT distribution. To address this, various conditioning mechanisms have been proposed to guide flow matching models for controlled generation [35–37].

In this study, we adopt a widely used strategy in conditional generative modeling, where the CBCT image input ( $y$ ) is concatenated with the flow sample ( $x_t$ ) along the channel as a static guidance during the velocity field approximation [25]. With the introduced conditioning input, the velocity estimator in flow matching changes from  $v_{t,\theta}(x_t)$  to  $v_{t,\theta}(x_t, y)$ . The modified workflow was shown in Figure 1(b). The training and sampling algorithms of the conditional flow matching model for CBCT-based synthetic CT are summarized in Algorithms 1 and 2.

---

**Algorithm 1** Flow Matching Training Procedure

---

- 1: **while** not converged **do**
  - 2:   Sample  $(y, x_1)$  from paired (CBCT, dpCT) dataset
  - 3:   Sample  $t$  from  $\mathcal{U}[0, 1]$
  - 4:   Sample  $x_0$  from Gaussian distribution
  - 5:   Set  $x_t = t \cdot x_1 + (1 - t) \cdot x_0$
  - 6:   Compute loss  $\mathcal{L}_{\text{CFM}}^{\text{OT}} = \|v_{t,\theta}(x_t, y) - (x_1 - x_0)\|^2$
  - 7:   Update  $\theta$  via gradient descent on  $\mathcal{L}_{\text{CFM}}^{\text{OT}}$
  - 8: **end while**
- 

---

**Algorithm 2** Euler Sampling

---

- 1: Set  $t = 0$
  - 2: Set step size  $\Delta t = \frac{1}{N}$
  - 3: Sample  $x_0$  from Gaussian distribution
  - 4: **for**  $k = 0$  to  $N - 1$  **do**
  - 5:    $x_{t+\Delta t} = x_t + \Delta t \cdot v_{t,\theta}(x_t, y)$
  - 6:    $t = t + \Delta t$
  - 7: **end for**
  - 8: **return**  $x_1$
- 

## 2.5 Comparison Studies

In the comparison studies, we include as a baseline the results obtained from a conditional diffusion probabilistic model (cDDPM) trained with 1000 denoising steps [25]. By comparing our flow matching formulations against the 1000-step cDDPM baseline, we are able to assess the behavior of flow-based methods in relation to a well-established diffusion approach, thereby situating our study within the broader context of generative modeling for CBCT-to-CT translation.

A major difference between the flow matching framework and the denoising diffusion models is the remarkable flexibility it offers in specification of the initial distribution. Traditional generative models, such as the variational autoencoders or denoising diffusion-based approaches, typically rely on simple priors (e.g., isotropic Gaussian) as the starting point of the generative process in order to facilitate mathematical tractability. The flow matching, by contrast, imposes no such restriction: the initial distribution  $p_0$  can, in principle, be chosen freely, as long as it is amenable to sampling. This property provides substantial modeling flexibility, since it allows the generative process to begin from a distribution that is already semantically or structurally close to the target distribution.

In this work, we take advantage of this property for methodological comparison by directly initializing the probability path from the empirical distribution of CBCT images, rather than adopting a synthetic prior such as Gaussian noise. Starting from the CBCT samples allows us to investigate how flow matching behaves when the source distribution is already structurally similar to the target CT distribution, rather than being completely unrelated. We emphasize that this choice of design is not necessarily intended to yield superior performance; rather, it highlights a distinctive modeling option enabled by flow matching. By examining both

Gaussian-to-CT and CBCT-to-CT formulations, we aim to provide a clearer picture of how the choice of initial distribution may influence the training dynamics and the generative mapping learned by the model.

To further examine the role of the initial distribution and conditional information in flow matching, we adopt two complementary strategies for comparison [38, 39]. In the first strategy (**CBCT w/o Concat**), we directly construct the flow from the CBCT distribution to the CT distribution, thereby treating CBCT as the starting point of the probability path, as shown in Figure 2(a). In the second strategy (**CBCT w/ Concat**), we build upon this formulation by additionally concatenating the CBCT image at each time step as an explicit conditioning input to the neural vector field, as depicted in Figure 2(b). This conditional variant allows the model to incorporate structural information from CBCT more explicitly during the flow evolution, offering a different perspective on how the source modality can be utilized in the generative process. Together, these two strategies provide a basis for systematically investigating how the choice of initialization and conditioning influences the learned mapping from CBCT to CT. The training and inference stages of these two methods are summarized in Algorithms 3–6.

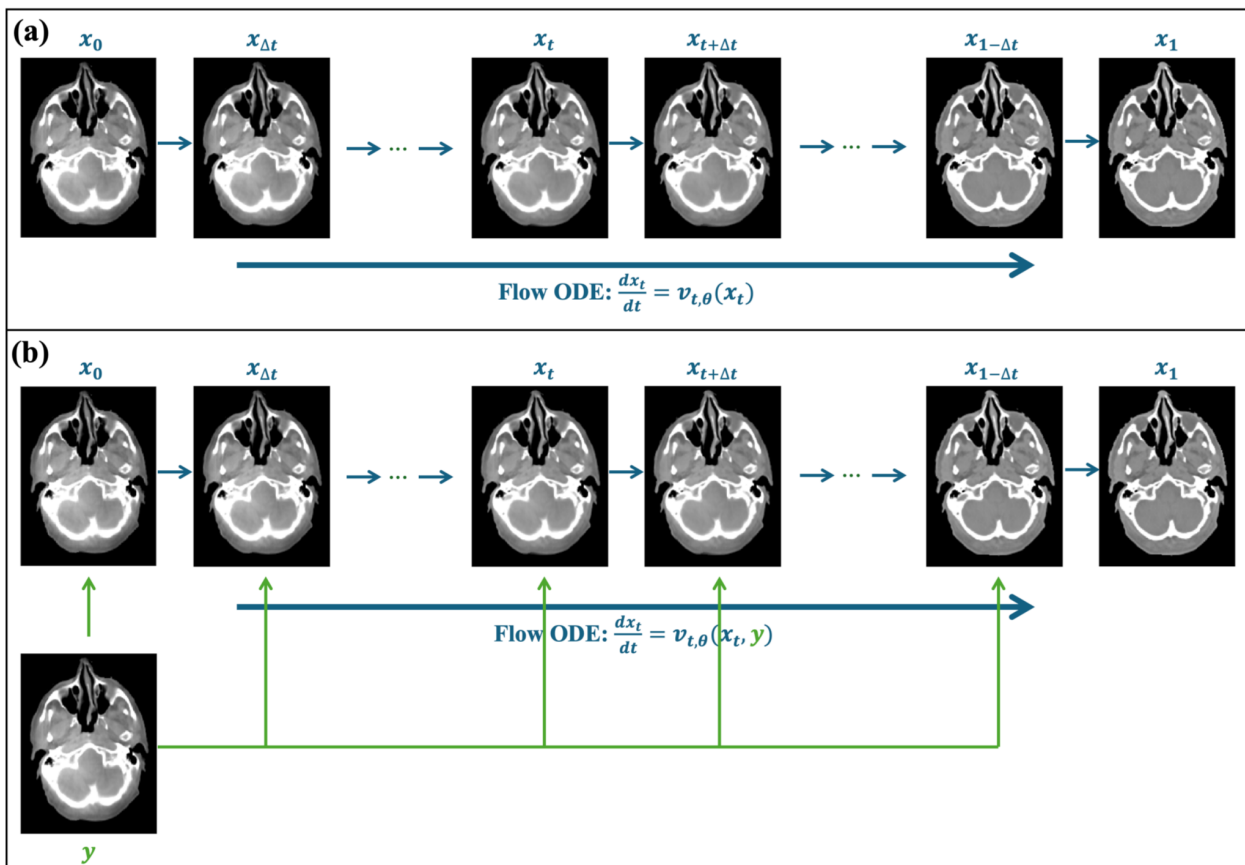


Figure 2: Workflows of (a) CBCT w/o Concat and (b) CBCT w/ Concat flow matching models for synthetic CT generation from CBCT.

To systematically evaluate these strategies, we examine the quality of generated CT images under different discretization granularities in the sampling stage. Specifically, for

---

**Algorithm 3** Flow Matching Training Procedure of (CBCT w/o Concat) Strategy

---

```

1: while not converged do
2:   Sample  $(x_0, x_1)$  from paired (CBCT, dpCT) dataset
3:   Sample  $t$  from  $\mathcal{U}[0, 1]$ 
4:   Set  $x_t = t \cdot x_1 + (1 - t) \cdot x_0$ 
5:   Compute loss  $\mathcal{L}_{\text{CFM}}^{\text{OT}} = \|v_{t,\theta}(x_t) - (x_1 - x_0)\|^2$ 
6:   Update  $\theta$  via gradient descent on  $\mathcal{L}_{\text{CFM}}^{\text{OT}}$ 
7: end while

```

---



---

**Algorithm 4** Euler Sampling of (CBCT w/o Concat) Strategy

---

```

1: Set  $t = 0$ 
2: Set step size  $\Delta t = \frac{1}{N}$ 
3: Sample  $x_0$  from CBCT distribution
4: for  $k = 0$  to  $N - 1$  do
5:    $x_{t+\Delta t} = x_t + \Delta t \cdot v_{t,\theta}(x_t)$ 
6:    $t = t + \Delta t$ 
7: end for
8: return  $x_1$ 

```

---



---

**Algorithm 5** Flow Matching Training Procedure of (CBCT w/ Concat) Strategy

---

```

1: while not converged do
2:   Sample  $(x_0, x_1)$  from paired (CBCT, dpCT) dataset
3:   Sample  $t$  from  $\mathcal{U}[0, 1]$ 
4:   Set  $x_t = t \cdot x_1 + (1 - t) \cdot x_0$ 
5:   Compute loss  $\mathcal{L}_{\text{CFM}}^{\text{OT}} = \|v_{t,\theta}(x_t, x_0) - (x_1 - x_0)\|^2$ 
6:   Update  $\theta$  via gradient descent on  $\mathcal{L}_{\text{CFM}}^{\text{OT}}$ 
7: end while

```

---



---

**Algorithm 6** Euler Sampling of (CBCT w/ Concat) Strategy

---

```

1: Set  $t = 0$ 
2: Set step size  $\Delta t = \frac{1}{N}$ 
3: Sample  $x_0$  from CBCT distribution
4: for  $k = 0$  to  $N - 1$  do
5:    $x_{t+\Delta t} = x_t + \Delta t \cdot v_{t,\theta}(x_t, x_0)$ 
6:    $t = t + \Delta t$ 
7: end for
8: return  $x_1$ 

```

---

each strategy we report results obtained using Euler integration with  $N \in \{5, 10, 20\}$  steps. This allows us to assess how the number of integration steps influences the fidelity and stability of the synthesized images, and to compare the relative robustness of the two flow matching formulations under coarse versus fine discretization.

## 2.6 Implementation and Evaluation

A U-Net architecture with residual blocks, attention modules, and time embeddings was adopted for vector field estimation at each step. All experiments in this work were conducted using PyTorch 1.12 framework on an NVIDIA RTX Ada 6000 GPU with 48 GB memory. Training was terminated after  $1 \times 10^6$  iterations, which took approximately 10 hours for the brain and HN studies and 30 hours for the lung study. The sampling stage of a single slice consumed 29/86 seconds (brain and HN patients/lung patients) using the baseline cDDPM method with 1000 time steps, while it only took 0.09/0.25 seconds, 0.21/0.64 seconds, and 0.49/1.41 seconds using the flow matching model with 5, 10, and 20 time steps. The sampling time was averaged over all 500 testing slices.

To evaluate the performance of the generated sCT images, we computed the mean absolute error (MAE), peak signal-to-noise ratio (PSNR), and normalized cross-correlation (NCC) with respect to the reference images (dpCT). These metrics are mathematically defined as follows:

$$\text{MAE} = \frac{1}{N} \sum_{m,n} |\text{sCT}(m, n) - \text{REF}(m, n)| \quad (14)$$

$$\text{PSNR} = 10 \cdot \log_{10} \left( \frac{\text{MAX}^2}{\frac{1}{N} \sum_{m,n} (\text{sCT}(m, n) - \text{REF}(m, n))^2} \right) \quad (15)$$

$$\text{NCC} = \frac{1}{N} \sum_{m,n} \frac{(\text{sCT}(m, n) - \overline{\text{sCT}})(\text{REF}(m, n) - \overline{\text{REF}})}{\sigma_{\text{sCT}} \sigma_{\text{REF}}} \quad (16)$$

where  $\text{sCT}(m, n)$  and  $\text{REF}(m, n)$  denote the pixel values at location  $(m, n)$  in the sCT and reference images, and  $N$  is the total number of pixels of the image.  $\text{MAX}$  is the maximum pixel intensity of the image.  $\overline{\text{sCT}}$  and  $\overline{\text{REF}}$  are the mean intensities, and  $\sigma_{\text{sCT}}$  and  $\sigma_{\text{REF}}$  are the standard deviations of the sCT and reference images, respectively.

The MAE quantifies the voxel-wise HU discrepancy between the sCT and CT. PSNR evaluates the global intensity consistency, and NCC measures the structural similarity between the two images.

## 3 Results

### 3.1 Improvement of Visual Quality

The visual effect of artifact correction using the proposed method is illustrated in Figure 3 over the brain patient cases. Pronounced beam-hardening artifacts, originating from the

high-density bones, are evident in all the CBCT images, manifesting as the inhomogeneity in intensity within the brain region and blurred boundaries between the bone and adjacent soft tissue. In contrast, the CT images generated by our method exhibit a substantial reduction of those artifacts while faithfully preserving fine anatomical structures, including the contrast agent and the maxillary sinus. This improvement is expected to enhance the accuracy of downstream tasks such as organ segmentation.

Figures 4 and 5 illustrate the visual improvements achieved by the proposed sCT method in the studies of HN patient and lung patient. The CBCT images were heavily degraded by streaking artifacts caused by motion and the presence of metallic implants. For the first two slices, the proposed approach produced artifact-free reconstructions that closely resemble the corresponding dpCT images. Furthermore, for severely degraded slices affected by strong metal artifacts, such as the last two slices, the sCT images generated by the proposed method exhibit effective artifact suppression that are compared to the dpCT images.

### 3.2 Quantitative Analysis

Table 1 tabulates the quantitative results for acquired CBCT and synthetic CT using the proposed method. For the brain patient study, the flow-matching model improved the HU accuracy from MAE of 40.63 HU for CBCT to 26.02 HU, 25.84 HU, and 26.31 HU with 5, 10, and 20 time steps. PSNR was improved from 27.87 dB for CBCT and 32.35 dB, 32.43 dB, and 32.15 dB for sCT with 5, 10, and 20 time steps. The NCC was 0.98 for CBCT and 0.99 for all the sCT results. For the HN patient study, MAE decreased from 38.99 HU to 33.17 HU, 33.02 HU, and 33.42 HU for sCT using 5, 10, and 20 steps. PSNR was slightly improved while NCC kept the same. For the lung patient study, MAE decreased from 32.90 HU to 25.09 HU, 24.20 HU, and 24.34 HU for sCT using 5, 10, and 20 steps. PSNR and NCC were slightly improved.

### 3.3 Comparison Studies

The sCT images generated by different flow matching models (5 step) and baseline conditional DDPM are summarized in Figure 6. Their quantitative evaluation metrics were summarized in Table 2. Compared to the sCT generated from the proposed method, the results from comparing the flow matching models exhibited varying levels of residual artifacts (indicated by the red arrows), particularly in the cases where the CBCT input contained severe degradations such as metal-induced streaking and ring artifacts. A plausible explanation is that, unlike the proposed method which starts from pure noise, the flow matching formulations are initialized directly from heavily corrupted CBCT images, making it more challenging to suppress artifacts that are already strongly embedded in the image domain. In addition, for each type of flow matching model, the differences among results obtained with 5, 10, and 20 integration steps were relatively minor, as can be observed from the quantitative metrics in Table 2.

We conducted Welch’s  $t$ -test to compare the results of the 5-step flow matching model with those of the 1000-step cDDPM, 10-step flow matching, and 20-step flow matching models, as summarized in Table 2. The results indicate that the proposed method with 5, 10, and 20 steps exhibited no significant differences across all three metrics. In contrast,

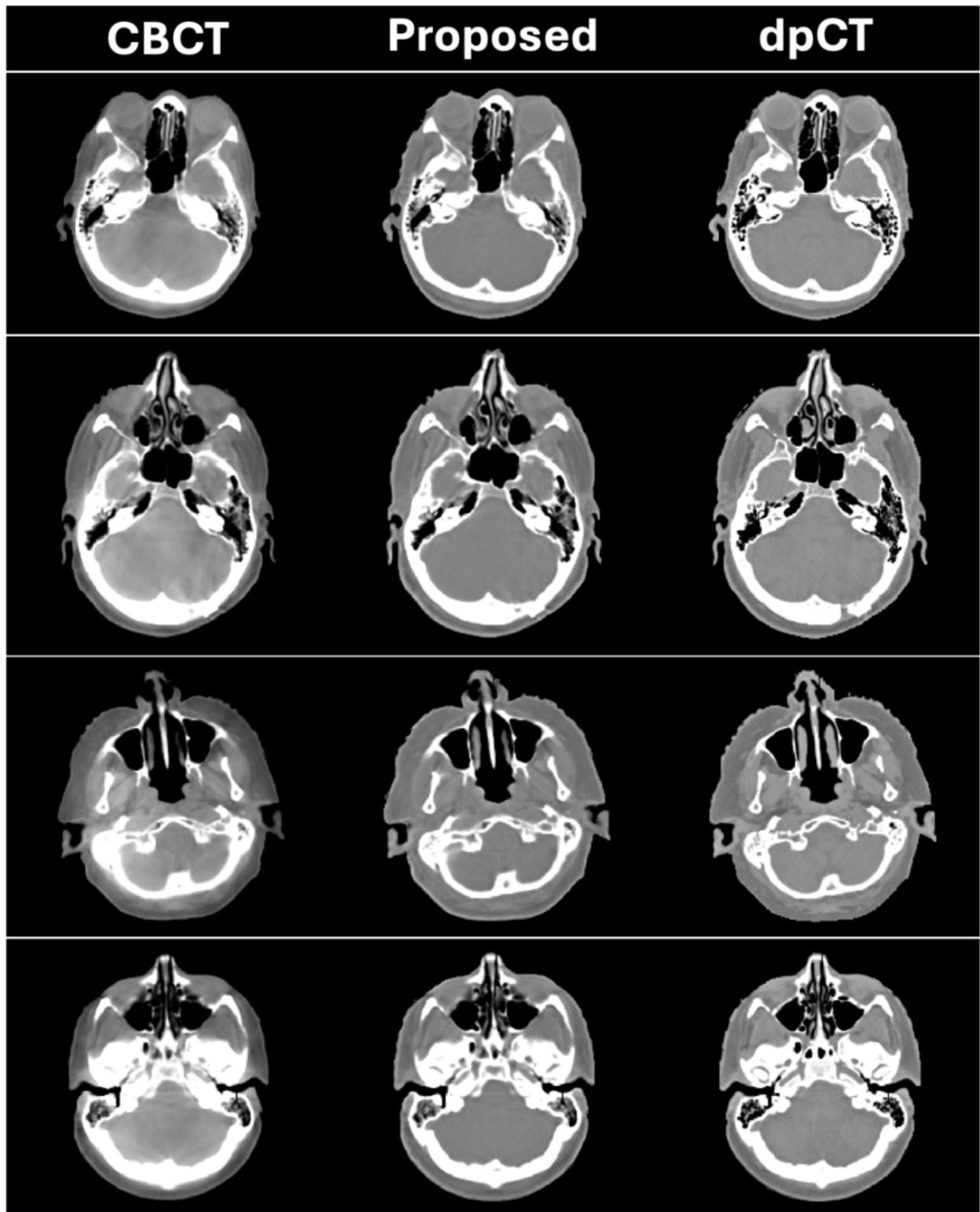


Figure 3: Visual effects of artifacts reduction in the study of brain patient. Left to right: CBCT, sCT generated by the proposed flow-matching model (5 step), and reference dpCT, respectively. Display window: [-500 500] HU.

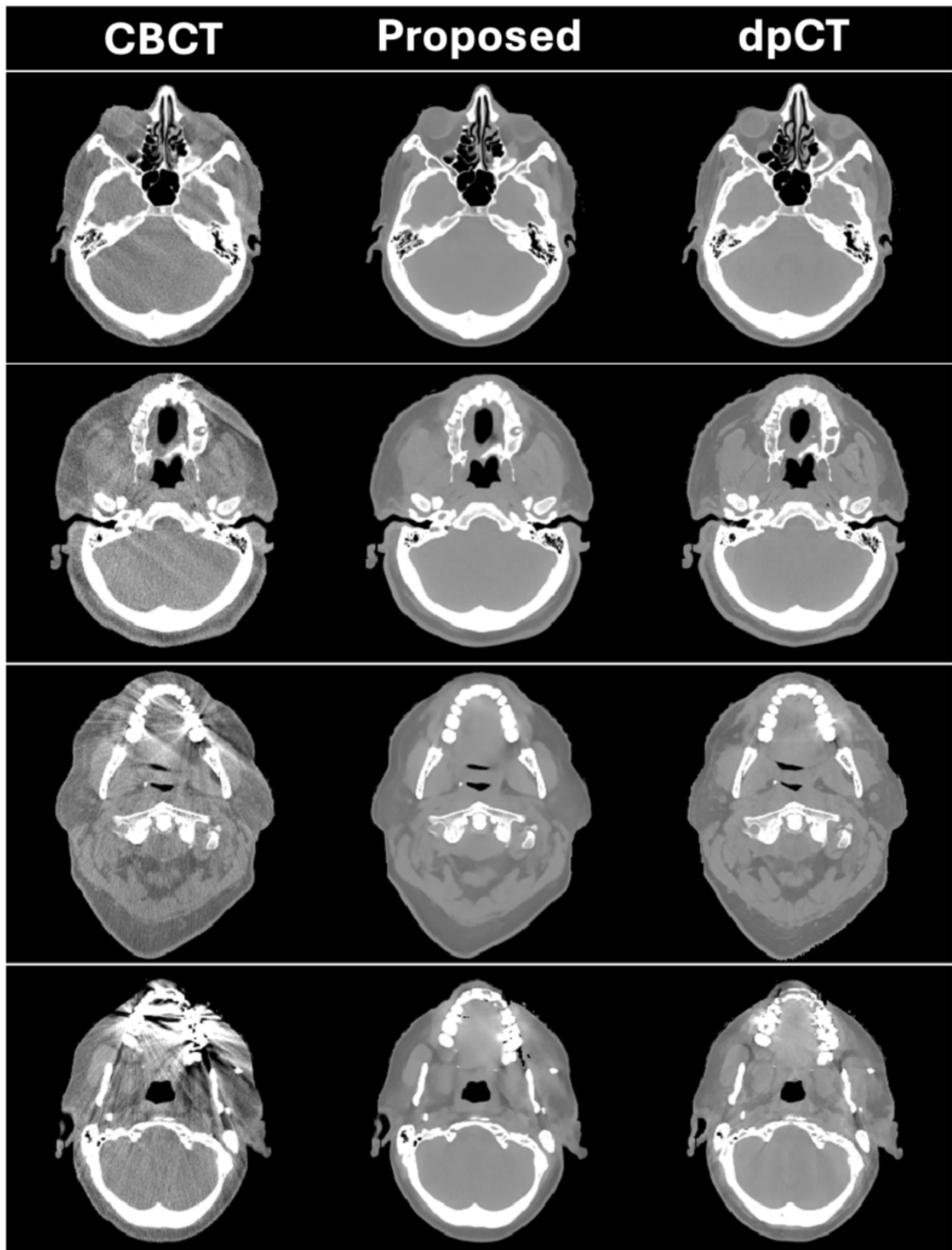


Figure 4: Visual effects of artifacts correction in the study of HN patient. Left to right: CBCT, sCT generated by the proposed flow-matching model (5 step), and reference dpCT, respectively. Display window: [-500 500] HU.

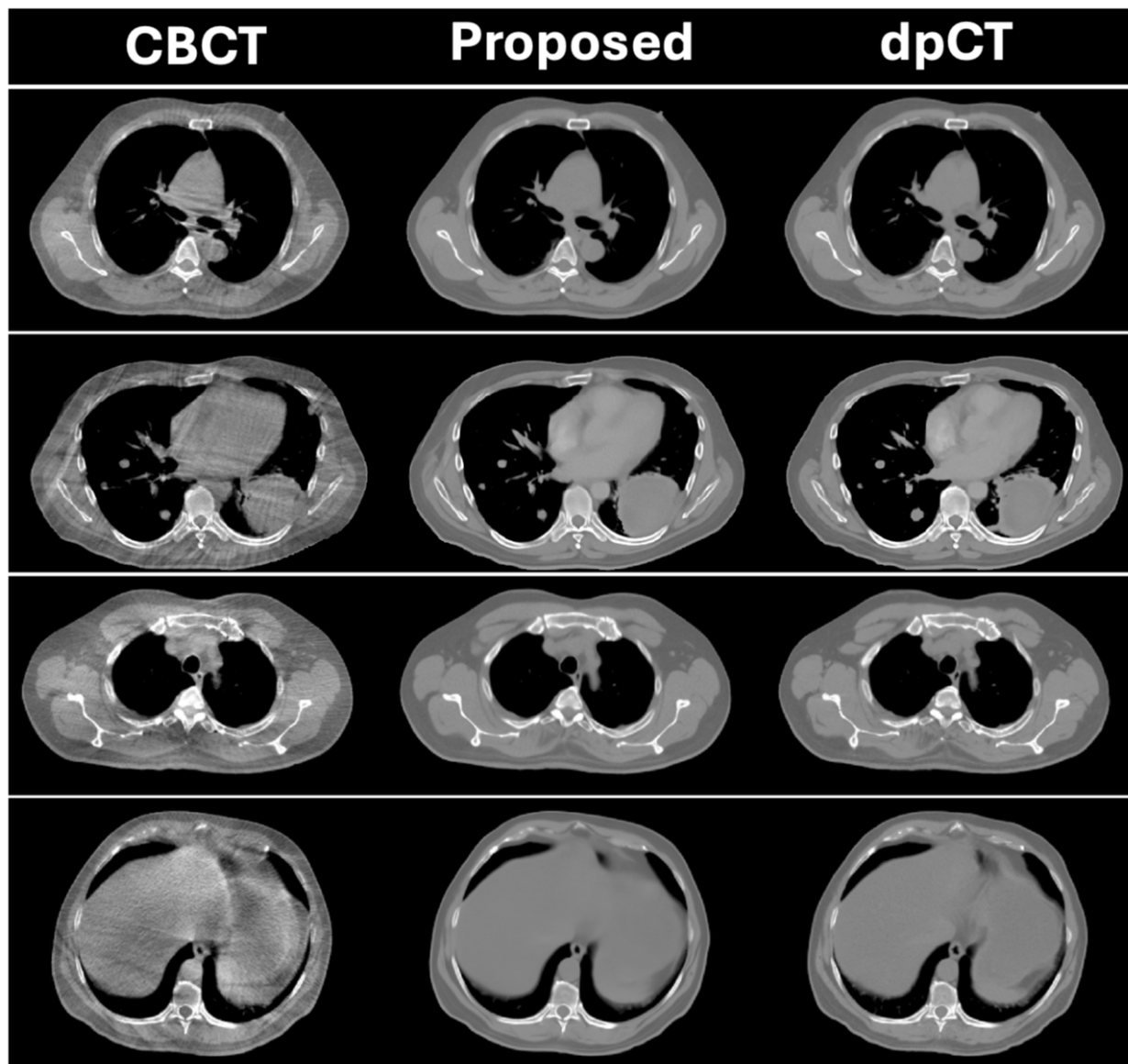


Figure 5: Visual effects of artifacts correction in the lung cohort. Left to right: CBCT, sCT generated by the proposed flow-matching model (5 step), and reference dpCT, respectively. Display window: [-500 500] HU.

Table 1: Quantitative metrics (mean  $\pm$  std) of the sCT using different methods.

Method	MAE (HU)			PSNR (dB)			NCC		
	Brain	HN	Lung	Brain	HN	Lung	Brain	HN	Lung
CBCT	40.63 $\pm$ 12.71	38.99 $\pm$ 14.07	32.90 $\pm$ 11.45	27.87 $\pm$ 2.20	27.00 $\pm$ 1.98	30.48 $\pm$ 2.36	0.98 $\pm$ 0.01	0.98 $\pm$ 0.01	0.98 $\pm$ 0.01
cDDPM (1000-Step)	25.99 $\pm$ 11.84	32.56 $\pm$ 12.86	24.68 $\pm$ 8.27	30.49 $\pm$ 3.73	27.65 $\pm$ 2.41	31.78 $\pm$ 2.14	0.99 $\pm$ 0.01	0.98 $\pm$ 0.01	0.99 $\pm$ 0.01
Proposed (5-Step)	26.02 $\pm$ 8.65	33.17 $\pm$ 9.74	25.09 $\pm$ 6.60	32.35 $\pm$ 3.42	28.68 $\pm$ 2.32	32.81 $\pm$ 2.35	0.99 $\pm$ 0.01	0.98 $\pm$ 0.01	0.99 $\pm$ 0.01
Proposed (10-Step)	25.84 $\pm$ 8.60	33.02 $\pm$ 9.73	25.20 $\pm$ 6.58	32.43 $\pm$ 3.41	28.78 $\pm$ 2.35	32.85 $\pm$ 2.43	0.99 $\pm$ 0.01	0.98 $\pm$ 0.01	0.99 $\pm$ 0.01
Proposed (20-Step)	26.31 $\pm$ 8.63	33.42 $\pm$ 9.77	24.34 $\pm$ 6.55	32.15 $\pm$ 3.33	28.61 $\pm$ 2.31	32.79 $\pm$ 2.31	28.61 $\pm$ 2.31	0.99 $\pm$ 0.01	0.98 $\pm$ 0.01
CBCT w/o Concat (5-Step)	27.30 $\pm$ 8.80	35.54 $\pm$ 10.43	25.01 $\pm$ 8.29	31.18 $\pm$ 2.99	28.26 $\pm$ 2.22	32.93 $\pm$ 2.62	0.99 $\pm$ 0.01	0.98 $\pm$ 0.01	0.99 $\pm$ 0.01
CBCT w/o Concat (10-Step)	27.61 $\pm$ 8.84	35.99 $\pm$ 10.67	25.27 $\pm$ 8.43	31.07 $\pm$ 2.97	28.20 $\pm$ 2.21	32.89 $\pm$ 2.62	0.99 $\pm$ 0.01	0.98 $\pm$ 0.01	0.99 $\pm$ 0.01
CBCT w/o Concat (20-Step)	27.79 $\pm$ 8.86	36.18 $\pm$ 10.68	25.47 $\pm$ 8.54	31.01 $\pm$ 2.96	28.15 $\pm$ 2.19	32.86 $\pm$ 2.63	0.99 $\pm$ 0.01	0.98 $\pm$ 0.01	0.99 $\pm$ 0.01
CBCT w/ Concat (5-Step)	27.18 $\pm$ 10.02	35.26 $\pm$ 12.69	25.68 $\pm$ 9.34	30.57 $\pm$ 2.67	28.02 $\pm$ 2.23	32.02 $\pm$ 2.65	0.99 $\pm$ 0.01	0.98 $\pm$ 0.01	0.99 $\pm$ 0.01
CBCT w/ Concat (10-Step)	27.11 $\pm$ 10.04	35.60 $\pm$ 12.72	25.31 $\pm$ 9.67	30.56 $\pm$ 2.68	27.96 $\pm$ 2.22	32.13 $\pm$ 2.63	0.99 $\pm$ 0.01	0.98 $\pm$ 0.01	0.99 $\pm$ 0.01
CBCT w/ Concat (20-Step)	28.21 $\pm$ 9.16	36.04 $\pm$ 12.89	25.57 $\pm$ 9.42	30.12 $\pm$ 2.63	27.87 $\pm$ 2.22	32.07 $\pm$ 2.61	0.99 $\pm$ 0.01	0.98 $\pm$ 0.01	0.99 $\pm$ 0.01

when compared with the 1000-step cDDPM, the 5-step flow matching model showed no significant difference in MAE, but achieved significantly better performance in both PSNR and NCC.

Table 2: Results of significance tests ( $p$ -value).

Comparison	MAE			PSNR			NCC		
	Brain	HN	Lung	Brain	HN	Lung	Brain	HN	Lung
Proposed (5-Step) vs. cDDPM (1000- Step)	0.57	0.40	0.43	<0.01	<0.01	<0.01	<0.01	<0.01	<0.01
Proposed (5-Step) vs. Proposed (10- Step)	0.74	0.81	0.52	0.69	0.51	0.23	0.66	0.34	0.61
Proposed (5-Step) vs. Proposed (20- Step)	0.59	0.68	0.31	0.35	0.61	0.34	0.51	0.58	0.42

## 4 Discussion

This study formulated CBCT-based CT synthesis under the conditional flow matching framework. To the best of our knowledge, this study represents the first attempt to perform CBCT-based CT synthesis using a flow matching-based generative model. Unlike denoising diffusion model-based methods, the proposed method efficiently generates enhanced-quality sCT images with significantly reduced sampling steps, thus reducing computational cost while maintaining or even improving the quality of generated sCT images.

One of the major limitations of this study is the supervised learning schemes employed for medical image translation. The supervised learning method relies on exactly matched image pairs, which are often unavailable in practice. For instance, it is infeasible to obtain paired CBCT-dpCT images from the same patient both with and without metal artifacts. Moreover, in radiotherapy practice, the anatomical changes such as tumor shrinkage, weight loss, or posture variation across treatment sessions further increase the mismatch between pCT and CBCT, making precise registration unattainable and thereby preventing the construction of exactly matched training pairs. In this context, it should be noticed that the quantitative comparisons between sCT and dpCT should be interpreted with caution, since the dpCT is not anatomically identical to the CBCT and may itself contain artifacts, whereas the sCT may be closer to the ground truth image.

It is also of interest to further explore the feasibility of flow matching models for sCT generation without CBCT and dpCT data pairs. There have been several recent attempts to leverage the Bayesian formulations in conjunction with diffusion models to achieve unsupervised image generation and reconstruction [26, 40]. While these approaches provide elegant approaches under the diffusion modeling framework, their underlying mathematical principles differ fundamentally from those of flow matching. Moreover, the flow matching

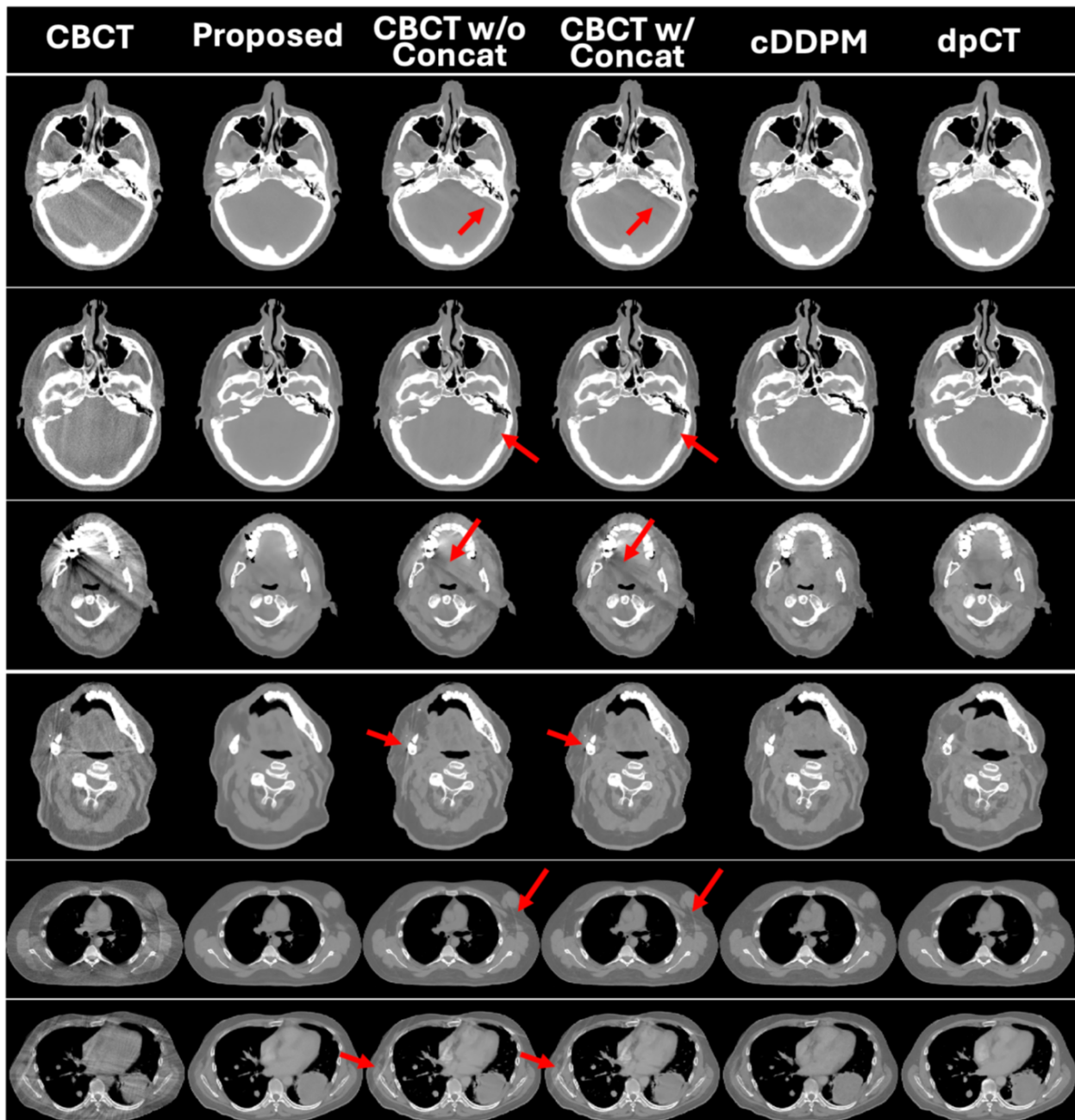


Figure 6: Results of sCT generated by different flow matching models (5 step) and baseline cDDPM (1000 step). Red arrows indicate the residual artifacts on sCT produced by compared flow matching models. Display window:  $[-500 \ 500]$  HU.

often operates with a relatively small number of integration steps, which may further complicate the incorporation of data consistency strategies. As a result, the Bayesian–diffusion strategies cannot be directly transferred to the flow matching setting. Developing analogous formulations that are compatible with the flow matching paradigm remains an open problem and will be an interesting direction for future investigation.

In this work, the proposed flow-matching model is implemented on 2D slices and does not employ any patch extraction strategy. While this choice of design simplifies training and reduces computational cost, it inevitably limits the model’s ability to fully capture 3D anatomical context. It is therefore reasonable to expect that a 3D latent-space or patch-based model [41], which can exploit volumetric information and spatial correlations across slices, would yield improved structural fidelity and more consistent preservation of anatomical continuity. Incorporating such 3D modeling strategies represents a promising direction for future work.

In this work, the sampling stage of the flow-based model was implemented using the explicit Euler solver to numerically integrate the underlying ODE. The Euler integration is simple and efficient, but it is also a first-order method and may introduce discretization bias while only a limited number of steps are being employed. More advanced solvers, such as higher-order Runge–Kutta methods, adaptive-step solvers, or predictor–corrector schemes, could potentially improve the trade-off between computational cost and sample fidelity. A systematic investigation of how different ODE solvers affect both the visual quality of the synthesized CT images and the stability of the sampling process will be pursued in future work.

## 5 Conclusions

In this study, we proposed a conditional flow matching framework for synthetic CT directly from CBCT inputs. The synthetic CT images demonstrated improved HU accuracy and exhibited substantially fewer artifacts compared to the original CBCT images, which may facilitate more direct CBCT-based organ segmentation and treatment replanning. Overall, the proposed method may extend the quantitative utility of CBCT and strengthens its potential role in the clinical workflow of direct CBCT-guided adaptive radiotherapy.

## References

- [1] A. Haworth, A. Paneghel, A. Herschtal, G. Duchesne, S. Williams, K. H. Tai, T. Kron, P. Roxby, S. Soteriou, M. Laferlita, and F. Foroudi, “Verification of target position in the post-prostatectomy cancer patient using cone beam CT,” *Journal of Medical Imaging and Radiation Oncology* **53**, 212–220 (2009).
- [2] R. Schulze, U. Heil, D. Groß, D. D. Bruellmann, E. Dranischnikow, U. Schwanecke, and E. Schömer, “Artefacts in CBCT: a review,” *Dentomaxillofacial Radiology* **40**, 265–273 (2011).

- [3] P. S. Cho, R. H. Johnson, and T. W. Griffin, "Cone-beam CT for radiotherapy applications," *Physics in Medicine & Biology* **40**, 1863–1883 (1995).
- [4] J. F. Barrett and N. Keat, "Artifacts in CT: Recognition and Avoidance," *RadioGraphics* **24**, 1679–1691 (2004).
- [5] H. Wang, L. Dong, M. F. Lii, A. L. Lee, R. de Crevoisier, R. Mohan, J. D. Cox, D. A. Kuban, and R. Cheung, "Implementation and validation of a three-dimensional deformable registration algorithm for targeted prostate cancer radiotherapy," *International Journal of Radiation Oncology\*Biophysics* **61**, 725–735 (2005).
- [6] S. Kida, S. Kaji, K. Nawa, T. Imae, T. Nakamoto, S. Ozaki, T. Ohta, Y. Nozawa, and K. Nakagawa, "Visual enhancement of Cone-beam CT by use of CycleGAN," *Medical Physics* **47**, 998–1010 (2020).
- [7] J. H. Siewerdsen, D. J. Moseley, B. Bakhtiar, S. Richard, and D. A. Jaffray, "The influence of antiscatter grids on soft-tissue detectability in cone-beam computed tomography with flat-panel detectors," *Medical Physics* **31**, 3506–3520 (2004).
- [8] L. Zhu, Y. Xie, J. Wang, and L. Xing, "Scatter correction for cone-beam CT in radiation therapy," *Medical Physics* **36**, 2258–2268 (2009).
- [9] W. Cai, R. Ning, and D. Conover, "Scatter correction using beam stop array algorithm for cone-beam CT breast imaging," in *Medical Imaging 2006: Physics of Medical Imaging*, volume 6142 of Proc. SPIE, pages 1157–1165, 2006.
- [10] Y. Xu, T. Bai, H. Yan, L. Ouyang, J. Wang, Y. Hu, X. Jia, and S. Jiang, "A practical cone-beam CT scatter correction method with optimized Monte Carlo simulations for image-guided radiation therapy," *Physics in Medicine & Biology* **60**, 3567–3587 (2015).
- [11] B. Bechara, W. S. Moore, C. A. McMahan, and M. Noujeim, "Metal artefact reduction with cone beam CT: an in vitro study," *Dentomaxillofacial Radiology* **41**, 248–253 (2012).
- [12] Y. Li, J. Garrett, and G.-H. Chen, "Reduction of beam hardening artifacts in cone-beam CT imaging via SMART-RECON algorithm," in *Medical Imaging 2016: Physics of Medical Imaging*, volume 9783 of Proc. SPIE, pages 225–231, 2016.
- [13] S. Xie, W. Zhuang, and H. Li, "An energy minimization method for the correction of cupping artifacts in cone-beam CT," *Journal of Applied Clinical Medical Physics* **17**, 307–319 (2016).
- [14] M. Sun and J. Star-Lack, "Improved scatter correction using adaptive scatter kernel superposition," *Physics in Medicine & Biology* **55**, 6695–6720 (2010).
- [15] L. Gao, K. Xie, J. Sun, A. Wu, Y. Zhang, Y. Chen, X. Liu, X. Yang, J. Sun, P. Liang, J. Zhou, J. Wu, H. Yan, and L. Ren, "Streaking artifact reduction for CBCT-based synthetic CT generation in adaptive radiotherapy," *Medical Physics* **49**, 5612–5626 (2022).

- [16] Y. Nomura, Q. Xu, H. Shirato, S. Shimizu, and L. Xing, "Projection-domain scatter correction for cone beam computed tomography using a residual convolutional neural network," *Medical Physics* **46**, 3142–3155 (2019).
- [17] L. Chen, X. Liang, C. Shen, S. Jiang, and J. Wang, "Synthetic CT generation from CBCT images via deep learning," *Medical Physics* **47**, 1115–1125 (2020).
- [18] L. Chen, X. Liang, C. Shen, D. Nguyen, S. Jiang, and J. Wang, "Synthetic CT generation from CBCT images via unsupervised deep learning," *Physics in Medicine & Biology* **66**, 115019 (2021).
- [19] J. Harms, Y. Lei, T. Wang, R. Zhang, J. Zhou, X. Tang, W. J. Curran, T. Liu, and X. Yang, "Paired cycle-GAN-based image correction for quantitative cone-beam computed tomography," *Medical Physics* **46**, 3998–4009 (2019).
- [20] X. Liang, L. Chen, D. Nguyen, Z. Zhou, X. Gu, M. Yang, and J. Wang, "Generating synthesized computed tomography (CT) from cone-beam computed tomography (CBCT) using CycleGAN for adaptive radiotherapy," *Physics in Medicine & Biology* **64**, 125002 (2019).
- [21] Y. Liu, Y. Lei, T. Wang, Y. Fu, X. Tang, W. J. Curran, T. Liu, and X. Yang, "CBCT-based synthetic CT generation using deep-attention cycleGAN for pancreatic adaptive radiotherapy," *Medical Physics* **47**, 2472–2483 (2020).
- [22] R. Ning, X. Tang, and D. Conover, "X-ray scatter correction algorithm for cone beam CT imaging," *Medical Physics* **31**, 1195–1202 (2004).
- [23] Y. Nomura, Q. Xu, H. Peng, H. Shirato, S. Shimizu, and L. Xing, "Modified fast adaptive scatter kernel superposition (mfASKS) correction and its dosimetric impact on CBCT-based proton therapy dose calculation," *Medical Physics* **47**, 190–200 (2020).
- [24] L. Yu, Z. Zhang, X. Li, and L. Xing, "Deep sinogram completion with image prior for metal artifact reduction in CT images," *IEEE Transactions on Medical Imaging* **40**, 228–238 (2020).
- [25] J. Peng et al., "CBCT-Based synthetic CT image generation using conditional denoising diffusion probabilistic model," *Medical Physics* **51**, 1847–1859 (2024).
- [26] J. Peng, Y. Gao, C.-W. Chang, R. Qiu, T. Wang, A. Kesarwala, K. Yang, J. Scott, D. Yu, and X. Yang, "Unsupervised Bayesian generation of synthetic CT from CBCT using patient-specific score-based prior," *Medical Physics* **52**, 2238–2246 (2025).
- [27] Y. Zhang et al., "Texture-preserving diffusion model for CBCT-to-CT synthesis," *Medical Image Analysis* **99**, 103362 (2025).
- [28] M. Li, X. Li, S. Safai, A. J. Lomax, and Y. Zhang, "Diffusion Schrödinger bridge models for high-quality MR-to-CT synthesis for proton treatment planning," *Medical Physics* (2025).

- [29] R. T. Chen, Y. Rubanova, J. Bettencourt, and D. K. Duvenaud, “Neural ordinary differential equations,” *Advances in Neural Information Processing Systems* **31** (2018).
- [30] C. Villani et al., *Optimal Transport: Old and New*, volume 338, Springer, 2008.
- [31] Y. Lipman, R. T. Chen, H. Ben-Hamu, M. Nickel, and M. Le, “Flow matching for generative modeling,” arXiv preprint arXiv:2210.02747 (2022).
- [32] X. Liu, C. Gong, and Q. Liu, “Flow straight and fast: Learning to generate and transfer data with rectified flow,” arXiv preprint arXiv:2209.03003 (2022).
- [33] A. Iserles, *A First Course in the Numerical Analysis of Differential Equations*, Number 44, Cambridge University Press, 2009.
- [34] Y. Lipman, M. Havasi, P. Holderrieth, N. Shaul, M. Le, B. Karrer, R. T. Chen, D. Lopez-Paz, H. Ben-Hamu, and I. Gat, “Flow matching guide and code,” arXiv preprint arXiv:2412.06264 (2024).
- [35] P. Esser et al., “Scaling rectified flow transformers for high-resolution image synthesis,” in *Forty-first International Conference on Machine Learning*, 2024.
- [36] L. Yariv, O. Puny, O. Gafni, and Y. Lipman, “Mosaic-SDF for 3D generative models,” in *Proceedings of the IEEE/CVF Conference on Computer Vision and Pattern Recognition*, pages 4630–4639, 2024.
- [37] Q. Zheng, M. Le, N. Shaul, Y. Lipman, A. Grover, and R. T. Chen, “Guided flows for generative modeling and decision making,” arXiv preprint arXiv:2311.13443 (2023).
- [38] G.-H. Liu, A. Vahdat, D.-A. Huang, E. A. Theodorou, W. Nie, and A. Anandkumar, “I<sup>2</sup>SB: Image-to-Image Schrödinger Bridge,” arXiv preprint arXiv:2302.05872 (2023).
- [39] M. S. Albergo, M. Goldstein, N. M. Boff, R. Ranganath, and E. Vanden-Eijnden, “Stochastic interpolants with data-dependent couplings,” arXiv preprint arXiv:2310.03725 (2023).
- [40] H. Chung, J. Kim, M. T. Mccann, M. L. Klasky, and J. C. Ye, “Diffusion posterior sampling for general noisy inverse problems,” arXiv preprint arXiv:2209.14687 (2022).
- [41] R. Rombach, A. Blattmann, D. Lorenz, P. Esser, and B. Ommer, “High-Resolution Image Synthesis with Latent Diffusion Models,” in *Proceedings of the IEEE/CVF Conference on Computer Vision and Pattern Recognition (CVPR)*, pages 10684–10695, 2022.